https://doi.org/10.5194/egusphere-2026-2126
Preprint. Discussion started: 8 May 2026

Estimating the source altitude of auroral precipitation from dispersed Alfvén waves in the dayside ionosphere.

Etienne Gavazzi[1], Andres Spicher[1], Björn Gustavsson[1], Juha Vierinen[1], James Clemmons[2], Robert Pfaff[3], and Douglas Rowland[3]

[1]Department of Physics and Technology, UiT The Arctic University of Norway, Tromsø, Norway
[2]Department of Physics and Astronomy, University of New Hampshire, Durham, NH, USA
[3]NASA Goddard Space Flight Center, Greenbelt, MD, United States

Correspondence: Etienne Gavazzi (etienne.gavazzi@uit.no)

Abstract. The VISIONS-2 sounding rockets performed in-situ measurements of the active dayside auroral region. Numerous broadband dispersed signatures up to keV energies are visible in the electron electrostatic analyser data, typical of Alfvénic precipitation. In order to characterize the region where the particle are accelerated, we estimate source altitudes based on different fits of the observed energy–time dispersions. Additionally, a method based on pitch-angle–time dispersions is developed, which allows relaxing the assumption of simultaneous injection at all distances. Both approaches are found to yield similar source altitudes. For most of the analysed dispersed precipitation structures, these are found to lie between 1,000 and 3,000 km, and increase in height for larger electron energies. Further, variations are observed across events, suggesting different conditions in the acceleration region. Finally, a comparison with previous observational studies and theoretical predictions is performed, and our estimated source altitudes are found to be generally consistent with some of the inertial Alfvén wave velocity profiles, especially those related to lower plasma densities environments. Overall, the results presented here provide further detail about the Alfvénic auroral acceleration region on the dayside. The developed method also opens the possibility of inferring the plasma density profiles and essential wave parameters above the spacecraft.

1 Introduction

Alfvén waves are thought to be a significant driver of auroral precipitation, particularly for small-scales dynamic structures (e.g. Kataoka et al., 2021, and references therein). Using FAST spacecraft traversals of the polar regions, Chaston et al. (2007a) estimated Alfvén waves to power on average 25 to 39 % of the auroral electron energy, and even to be the dominant mechanism around the noon and midnight sectors under active conditions (e.g. substorms). As such, particle acceleration by Alfvén waves seems to be an important coupling mechanism between the magnetospheric and ionospheric systems, contributing to the dissipation of magnetospheric energy by accelerating electrons into the ionosphere (Wygant et al., 2000).

In order to interact and accelerate electrons along the field lines to auroral energies (hundreds of eV to several keV), Alfvén waves must carry a parallel electric field component. While impossible in the MHD limit, this becomes possible when the waves have small perpendicular scales and become dispersive (Stasiewicz et al., 2000). In magnetospheric plasmas where the electron thermal velocity $v_e = (2T_e/m_e)^{1/2}$ is greater than the Alfvén velocity $v_A = \frac{B_0}{(\mu_0 n_i m_i)^{1/2}}$, i.e. $v_A < v_e$, the waves

https://doi.org/10.5194/egusphere-2026-2126
Preprint. Discussion started: 8 May 2026

become dispersive at perpendicular scales on the order of the ion acoustic gyroradius $\rho_s = c_s/\Omega_i$ (Hasegawa, 1976), where $c_s = (T_e/m_i)^{1/2}$ is the ion acoustic speed and $\Omega_i = eB/m_i$ is the ion gyrofrequency. As kinetic effects dominate, these waves are commonly referred to as kinetic Alfvén waves (KAWs) (Stasiewicz et al., 2000). In plasmas where $v_A > v_e$, which is typically the case under 3-4 R_E (Earth radii), the waves become dispersive at perpendicular scales on the order of the electron inertial length (skin-depth) $\lambda_e = c/\omega_e$ (Goertz and Boswell, 1979), where $\omega_e = (ne^2/m_e\epsilon_0)^{1/2}$ is the plasma frequency. As inertial effects dominate, these waves are commonly referred to as inertial Alfvén waves (IAWs) (Stasiewicz et al., 2000). In both these regimes, dispersive Alfvén waves (DAWs) can accelerate electrons to energies up to $1v_A$ through Landau resonance (Chaston et al., 2003a; Lysak, 2023) and up to $2v_A$ through Fermi-like resonant processes (Kletzing, 1994; Chen et al., 2005; Watt et al., 2006), producing keV electrons.

The wave-particle interaction below a few Earth radii in the inertial regime has been extensively studied and modelled (Hui and Seyler, 1992; Kletzing, 1994; Kletzing and Hu, 2001; Chaston et al., 2002a, b; Watt et al., 2005; Watt and Rankin, 2007), confirming the ability of the Fermi-like resonance process to produce keV electron energies, as well as reproduce the morphology of observations. These simulations find the acceleration to high energies (keV) to take place around and above 5000 km (Kletzing and Hu, 2001; Chaston et al., 2003a). Other studies have also shown that KAWs above a few Earth radii were capable of accelerating electrons to several keV and to reproduce a morphology similar to observations made closer to the ionosphere (Watt and Rankin, 2010).

On the observational side, in-situ measurements from sounding rockets or satellite can be used to try to infer the location of wave-particle interaction. This identification can help constrain and better understand the underlying acceleration mechanisms, and ultimately improve our understanding of the energy transfer from the magnetosphere to the ionosphere. In time-energy spectrograms of the electron flux, signatures of Alfvénic precipitation are typically broadband in energy and dispersed in time, with higher-energy electrons arriving first and lower-energy electrons arriving later (Kletzing and Torbert, 1994; Andersson et al., 2002). It is important to note, however, that inverse dispersion (lower energies before higher energies) has also been reported (Cameron and Knudsen, 2016; Wu et al., 2021). These energy–time dispersions are frequently analysed to estimate the altitude of interaction using a method based on a linear fit of the electron arrival times (e.g. McFadden et al., 1987; Clemmons et al., 1994; Arnoldy et al., 1999; Lynch et al., 1999, 2012; Andersson et al., 2002; Tanaka et al., 2005; Motoba and Hirahara, 2016; Hirahara et al., 2024; Feltman et al., 2025; Michell et al., 2025). Source altitudes inferred with this method are typically on the order of several thousands of kilometers, consistent with results from IAWs modelling cited above. This method assumes that electrons at all energies were emitted simultaneously at one altitude. The limitations of this assumption for representing a moving wave-particle interaction are known (Andersson et al., 2002), and Tanaka et al. (2005) showed that higher-order quadratic curves provided a better fit of the energy–time dispersions they observed on the dayside. Feltman et al. (2025) recently repeated the method and reported the same findings for dispersions observed on the nightside. Compared to linear fits, quadratic fits allow the inferred source altitude to vary with energy, yielding a range of possible interaction altitudes, although still under the assumption of a simultaneous release from all altitudes.

In this study, dayside auroral precipitation observed by the Visualizing Ion Outflow via Neutral Atom Sensing-2 (VISIONS-2) sounding rocket mission is analysed, with the aim to help improving our understanding of the conditions around acceleration

https://doi.org/10.5194/egusphere-2026-2126
Preprint. Discussion started: 8 May 2026

processes related to DAWs. The rocket intersected numerous energy–time dispersed precipitation events (Gavazzi et al., 2026), on which we apply the classical linear fit, the quadratic fit proposed by Tanaka et al. (2005), as well as a logarithmic fit, and results from these methods are compared. In order to relax the assumption of simultaneous release at all energies inherent to these techniques, a method using observed pitch-angle–time dispersions to estimate independently the source altitudes for each energy is also introduced. The source altitudes obtained from the energy and pitch-angle methods applied to the same events are compared and evaluated. Source altitudes across events are then compared and discussed in the context of Alfvén speed profiles derived from density models and prior estimates of acceleration altitudes from other studies.

The outline of the paper is the following. Section 2 presents an overview of the observational data. Section 3 describes the different methods of source altitude estimation from energy–time dispersions (section 3.1) and pitch-angle–time dispersions (section 3.2). Section 4 present the results of the methods applied to different events. In section 5, the methods being used as well as the source altitudes being found are discussed.

2 Overview

The VISIONS-2 mission consists of a pair of sounding rockets launched from Ny-Ålesund, Svalbard, on 7 December 2018. The high-flyer (NASA 35.039) was launched at 11:06 UTC and the low flyer (NASA 35.040) was launched at 11:08 UTC, which corresponds to around 13.5 MLT. Both rockets flew towards the south-west through the active dayside auroral region (Takahashi et al., 2022). The high-flyer and the low-flyer reached an apogee of 806.6 km and 601.2 km, respectively. The low-flyer carried a top-hat electron electrostatic analyser (EESA) that measured the electron energy flux in time, energy and pitch-angle. The analyser swept through a series of 49 energy steps distributed exponentially from 3 eV to 28.6 keV, completing a full sweep in 50 ms. The instrument design (Carlson et al., 1982) allowed for each energy measurements to be realized simultaneously across 20 pitch-angle directions from 0 to 360°, with 0° corresponding to field-aligned down towards Earth and 180° corresponding to field-aligned up. A pitch-angle indexing offset in the instrument data was adjusted following Gavazzi et al. (2026).

To provide context, Figure 1a shows the differential electron energy flux plotted over energy and time for electrons with pitch-angle of 0° to 7.5°, for the whole flight. Figure 1b–g present a subset of that data from 328 s to 344 s after launch. Numerous broadband energy structures are visible between 331 s and 340 s in Figure 1b, with the shared characteristic that higher energy electrons are measured first followed by lower energy electrons, resulting in energy–time dispersions. The structures observed have peak energies ranging from a few hundreds of eV to a few keV and typical durations less than 0.5 s. Figure 1c, 1d and 1e show the differential electron energy flux at fixed energies (114, 525 and 1129 eV), plotted over pitch-angle and time. Horizontal white dashed lines mark pitch-angles of $\pm 90°$. Angles between these lines correspond to down-going electrons, while angles above and below correspond to up-going electrons. A band with no data is visible at 135° due to a dead channel. Numerous semicircular structures are visible in Figure 1d and Figure 1e (at 525 eV and 1129 eV), where field-aligned electrons are measured first, and the time-of-arrival increases with pitch-angle. These pitch-angle–time dispersions coincide with the energy–time dispersions observed in Figure 1b. The semicircular structures are not visible in Figure 1c (114 eV), but enhancements in the field-aligned flux (around 0°) can be observed at the same time as the structures

https://doi.org/10.5194/egusphere-2026-2126
Preprint. Discussion started: 8 May 2026

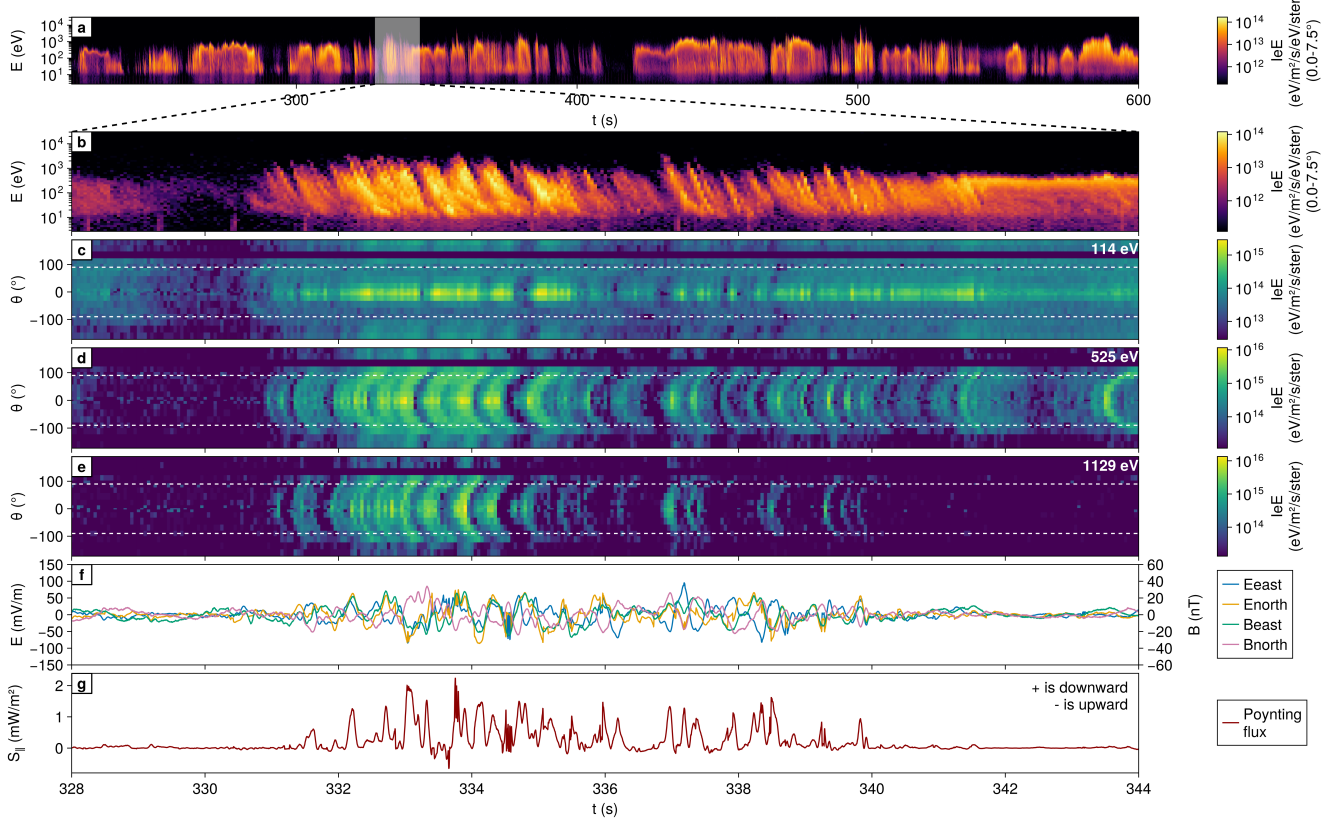

Figure 1. (a) Electron energy flux over time and energy, for 0–7.5° pitch-angle. (b–d) Electron energy flux over time and pitch-angle, different panels correspond to different energies (114, 525 and 1129 eV) as indicated in the top right corner of each panel. (e) Perpendicular components of the electric and magnetic fields. DC components have been filtered out. (f) Field-aligned Poynting flux. Positive values correspond to a downward flux into the ionosphere.

are seen in Figure 1d and 1e. To show coincident electromagnetic wave activity, Figure 1f presents the perpendicular electric and magnetic fields measured by another instrument onboard the rocket, with DC components removed using a high-pass filter. Figure 1g shows the field-aligned Poynting flux $S_{\parallel}$ calculated from the field measurements shown in Figure 1f. Positive values $S_{\parallel} > 0$, indicative of a downward energy flux into the ionosphere, are clearly visible in the time interval 331 s to 340 s when energy–time and pitch-angle–time dispersed structures are observed in Figure 1b, Figure 1d and Figure 1e. This is consistent with an Alfvénic acceleration of the precipitating electrons, and also indicates that not all the Poynting flux is dissipated by the wave-particle interaction.

https://doi.org/10.5194/egusphere-2026-2126
Preprint. Discussion started: 8 May 2026

3 Dispersions fitting

In the rest of this article, we refer to the path-length along a magnetic field line from ground as a *source altitude*. For the high-latitudes and altitude ranges considered here, the path-length along a magnetic field line and the geodetic height above ground differ by less than 1% (e.g. a distance of 10,000 km along a magnetic field line corresponds to an altitude above ground of approximately 9,900 km).

In the following sub-sections, we describe two classes of methods for estimating source altitude of Alfvénic precipitation. The first one is based on fitting energy–time dispersions, and the second uses pitch-angle–time dispersions. The combined results of both methods applied to dispersions measured by VISIONS-2 are shown in section 4.

3.1 Energy–time dispersions

Estimation of source altitude through a linear fit of the time-of-flight (TOF) slope of energy–time dispersions is a method widely used in the literature (e.g. McFadden et al., 1987; Clemmons et al., 1994; Arnoldy et al., 1999; Lynch et al., 1999, 2012; Andersson et al., 2002; Tanaka et al., 2005; Motoba and Hirahara, 2016; Hirahara et al., 2024; Feltman et al., 2025; Michell et al., 2025). It assumes that electrons of different energies are released simultaneously from a single altitude, so that differences in arrival time arise only from the differences in time-of-flight between electrons with different velocities. This assumption does not accurately represent the expected spatial and temporal characteristics of a wave-particle interaction, which is thought to happen over a wide range of altitudes as DAWs propagate downward toward the ionosphere (Kletzing and Hu, 2001). These limitations are known (e.g. Kletzing, 1994; Andersson et al., 2002; Tanaka et al., 2005; Feltman et al., 2025), but the method remains useful as it provides a single characteristic distance that can be compared across events and studies. Using the Akaike Information Criterion (AIC), Tanaka et al. (2005) showed that a 2nd order polynomial (quadratic curve) is frequently a better fit to the dispersion curves of the delay in arrival time Δt over the inverse of the electron velocity $(1/v)$ than the classical linear fit. This suggests that the relationship between arrival time and inverse velocity is not strictly linear, which is expected if acceleration occurs over a range of altitudes rather than at a single point (Tanaka et al., 2005). The fitted curve can then be differentiated to obtain a range of source altitudes varying with electron energy, though this still implies a simultaneous release at all energies over the range.

As shown in Figure 1, numerous distinct time–energy dispersed structure are visible in the VISIONS-2 data, to which the TOF fitting methods described above can be applied. Figure 2 presents an illustrative example using one event identified at around 338 s (Figure 1b). Figure 2a shows the energy–time dispersed structure. Measurements on either side of the structure (displayed with higher transparency) are excluded from the analysis, as we attribute them to adjacent precipitation. For each energy slice, the electron arrival time is determined by calculating the flux-weighted mean time. These mean values are marked with white dots in Figure 2a, and the white horizontal bars indicate the width in time of the structure as given by the square root of the weighted second moment calculated around each mean (standard deviation). Figure 2b shows the same mean arrival time, Δt, and estimated widths, plotted in Δt over $1/v$ space. The blue curve shows the best linear fit of the form $\Delta t = a + b(1/v)$, while the red curve shows the best quadratic fit of the form $\Delta t = a + b(1/v) + c(1/v)^2$ where a, b and c are

https://doi.org/10.5194/egusphere-2026-2126
Preprint. Discussion started: 8 May 2026

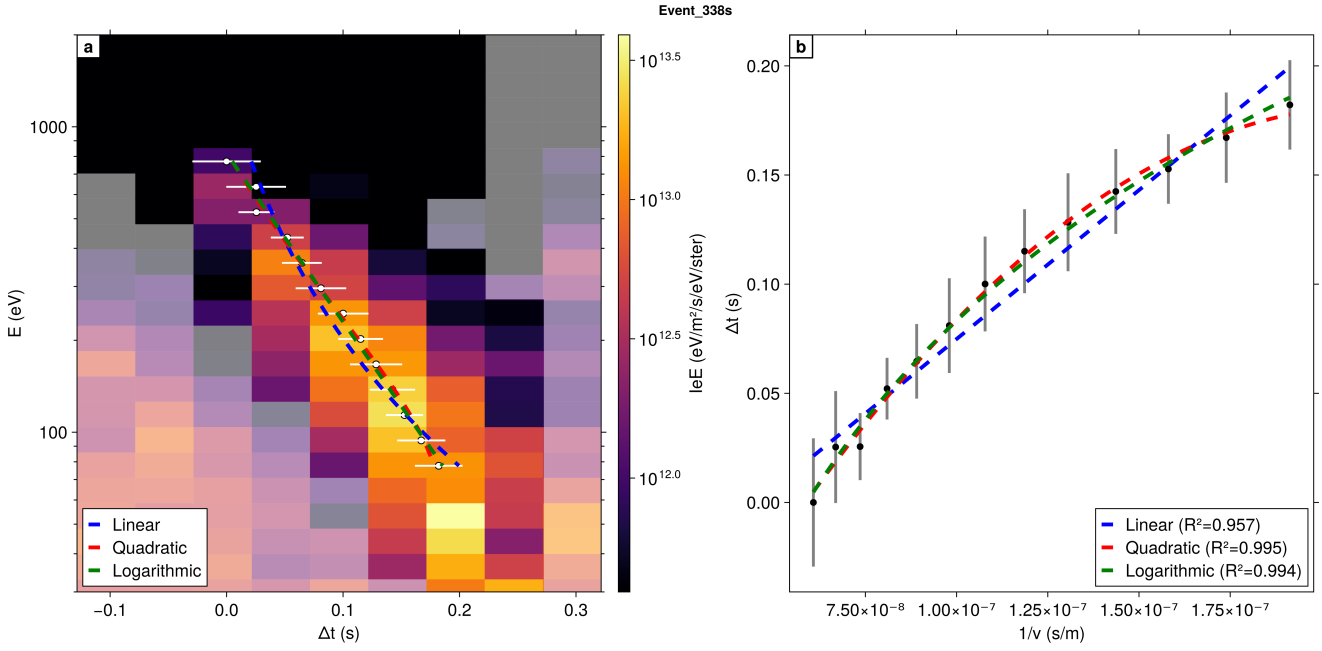

Figure 2. (a) Zoom-in on the energy-time dispersed structure visible in Figure 1b at 338 s. Data surrounding the structure and not taken into account in the analysis are shown with a high transparency. White dots indicate the mean arrival time Δt of each energy, and the white horizontal bars indicate the width in energy of the structure as given by the standard deviation around the mean. (b) Mean arrival times Δt plotted over corresponding $1/v$. Gray vertical bars indicate one standard deviation as in panel (a). The blue, red and green bars in both panels indicate respectively the best linear, quadratic and logarithmic fit of Δt over $1/v$.

the best fit parameters, following the approach proposed by Tanaka et al. (2005). In addition, we fit a logarithmic curve of the form $\Delta t = a - b\ln(1/v)$, shown in green in Figure 2. This curve corresponds to a straight line in an energy-time space plotted on a semi-log scale such as in Figure 2a, which seems to visually correspond well with several events in our dataset. Arrival times for energies under 70 eV are excluded from the analysis. Measurements at these lower energies are generally noisier, making the identification of well-defined peaks in arrival time more challenging. Tests made by varying the cut-off value from 50 eV to 100 eV did not change the overall trend of the results significantly, indicating that the analysis is not strongly sensitive to the exact value of this threshold. A more detailed discussion of this choice is provided in Section 4.

Following Tanaka et al. (2005) and Feltman et al. (2025), a range of source altitude can be estimated using the function $\mathcal{F}$ relating Δt and $\frac{1}{v}$ through $\Delta t = \mathcal{F}\left(\frac{1}{v}\right)$. Taking the derivative $\frac{d\mathcal{F}}{d\left(\frac{1}{v}\right)}$ provides an estimate of the source distance at any given $1/v$ via a local linear TOF approximation of the form $\Delta t = d\frac{1}{v}$, where d corresponds to the slope of the tangent of $\mathcal{F}$ at that point. For the linear fit, this slope is constant, yielding the same source altitude for all energies. In contrast, the slope varies with $1/v$ for the non-linear fits, resulting in different altitudes for different energies. Both methods, however, still rely on the assumption of an instantaneous electron release over the inferred altitude range.

https://doi.org/10.5194/egusphere-2026-2126
Preprint. Discussion started: 8 May 2026

3.2 Pitch-angle–time dispersions

Although the energy–time linear TOF method as described in the previous section is frequently used in studies, fewer have exploited pitch-angle–time dispersions for source altitude estimation. The advantage of such a method would be that, as long as the dispersions are visible across multiple energy channels, the source altitude could be estimated independently for each electron energy. This is a relaxation of the assumption of simultaneous release across energies that underlies the energy–time methods described in the previous section. For instance, Tanaka et al. (2005) attempted to estimate source altitudes from the different arrival times of electrons at 0° and 30° pitch-angle, but the resulting source altitude estimates carried large uncertainties (several thousands of kilometers), which were attributed to insufficient time and angular resolution. They concluded that measurements with higher resolution were necessary. The time resolution of our measurements (∼50 ms) is similar to theirs (∼41 ms), but the angular resolution of the EEAS onboard VISIONS-2 allows us to resolve clear pitch-angle–time dispersions across a higher number of pitch-angle channels (-70°, -45°, -20°, -5°, 0°, 5°, 20°, 45°, 75°) as seen in Figure 1.

Here, we test and further expand on the idea of using pitch-angle–time dispersions by developing and using a simple forward model, with two main components.

The first component simulates the propagation of electrons from a source altitude z_{source} to a measurement altitude z_{meas}. The electrons, all with the same kinetic energy, are launched simultaneously from z_{source} with a range of pitch-angles. The magnetic mirroring force is accounted for by conservation of the magnetic moment $\mu = \frac{m_e v_\perp^2}{2B}$, where variations in the field strength B along the field line are computed using the IGRF-14 model (International Association of Geomagnetism and Aeronomy, 2024), which is close to a dipole field model over the heights of interest. As such, the pitch-angle is allowed to evolve along the particle trajectory, which can change the total path-length.

The second component models the detector response. A Gaussian with width σ_t is centered on the computed time-of-arrival of each electron, representing an injection at source altitude extended in time. Electrons arriving within a certain pitch-angle and time window are then integrated to produce a simulated total count for each detector pixel. The time windows are 1 ms wide and repeated every 50 ms to reproduce the behaviour of the instrumental energy sweep. The pitch-angle window widths match the angular resolution of the instrument channels. Since the absolute time of injection is unknown, a free offset parameter t_{offset} is applied uniformly to all arrival times.

For each energy channel, electron trajectories are computed and the three model parameters z_{source}, σ_t and t_{offset} are varied. The advantage of this approach is that, unlike with the energy-time dispersion fits, each energy bin will have an independently fit release height and time. The best fitting values are found by minimizing the sum of squared errors (SSE) between the normalized observed and modelled pitch-angle–time dispersions. Because the intensity distribution across pitch-angle in the source population is not constrained by the model, each pitch-angle channel is normalized by its total flux count before computing the SSE. This normalization also mitigate potential differences in sensitivity between pitch-angle channels in the observed data. As a result, the optimization compares only the morphology of the pitch-angle–time dispersions, rather than their absolute amplitudes.

https://doi.org/10.5194/egusphere-2026-2126
Preprint. Discussion started: 8 May 2026

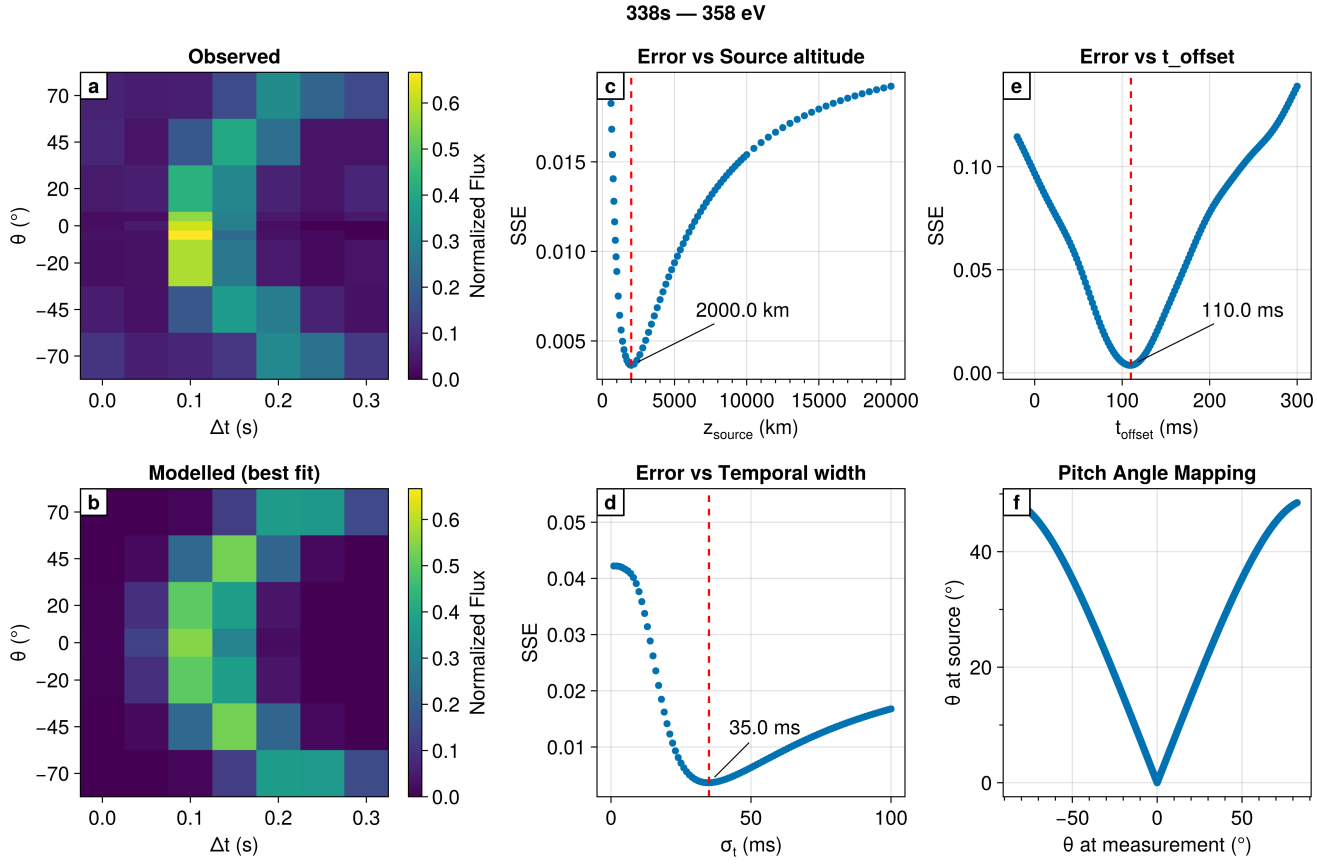

Figure 3. (a) Observed pitch-angle–time dispersion in the 358 eV slice of the event seen at 338 s in Figure 1. The total flux in each pitch-angle channel has been normalized to 1. (b) Best simulated dispersion by the forward model, as found by the minimization of the SSE. (c) Variation of the SSE over the parameter z_{source}, for the best values of σ_t and t_{offset}. (d) Variation of the SSE over the parameter σ_t for the best values of z_{source} and t_{offset}. (e) Variation of the SSE over the parameter t_{offset} for the best values of z_{source} and σ_t. (f) Relation between the pitch-angle of electrons at the source altitude and measurement altitude.

An example of the application of the forward model is shown in Figure 3. The event is the same as the one whose energy–time dispersion was presented in Figure 2, and the energy slice considered here is taken at 358 eV. Figure 3a shows the observed pitch-angle–time dispersion after normalization, while Figure 3b presents the best-fit modelled dispersion. Figures 3c–e illustrate the variation of the SSE as a function of each of the three model parameters z_{source}, σ_t and t_{offset}, with the remaining two others parameters held fixed at their best-fit values. The best-fit value of each parameter is indicated by a vertical dashed line and an annotation. Finally, Figure 3f shows the mapping between pitch-angles at the source altitude and those at the measurement altitude for the best-fit solution. In this example, electrons measured with a pitch-angle of 60° at the rocket altitude started with a pitch-angle of approximately 40° at the inferred source altitude.

https://doi.org/10.5194/egusphere-2026-2126
Preprint. Discussion started: 8 May 2026

Once the best-fitting parameters are found, the uncertainty in the estimated source altitude is obtained through a linearised uncertainty estimation (Aster et al., 2019). The parameter covariance matrix Σ_p is calculated as

$$\Sigma_p = \sigma_r^2 (J^T J)^{-1}$$

where σ_r is the root mean square difference between the observed and best-fit modelled dispersions, and J is the Jacobian matrix of the model evaluated around the best-fit parameters. The standard error on the source altitude is then the square root of the first diagonal element of Σ_p.

4 Source altitudes

We now apply the energy–time and pitch-angle–time dispersion fitting methods as described in the previous section to events measured by the rocket. Figure 4a shows the source altitude as a function of electron energy found with the different methods applied to the event at 338 s. This is the event that was used to describe the fitting methods in Figures 2 and 3. Figures 4b–f show results from other dispersed events, whose time in flight is indicated in the top-right corner of each panel. The blue, red, and green curves show results from respectively the linear, quadratic, and logarithmic energy–time TOF fits. For each event, the source altitude curve inferred from the best fitting model is indicated with a solid line while curves from the two others are dashed. Determining the best fitting model was done using the corrected Akaike Information Criterion (AICc) (Sugiura, 1978):

$$AICc = AIC + \frac{2k^2 + 2k}{n - k - 1} \tag{1}$$

where $AIC = 2k + n\ln(RSS/n)$ is the standard Akaike Information Criterion (Akaike, 1974) with unknown variance, RSS is the residual sum of squares, n is the number of data points, and k is the number of parameters in the model being fitted (e.g. 3 for the quadratic fit : a, b and c). We use the AICc correction in place of the AIC as the number of data points per event is small (regularly fewer than 15), which can cause the standard AIC to overly favour complex models (Cavanaugh and Neath, 2019).

The purple points show source altitudes estimated from the pitch-angle–time dispersion forward model, with errors bars representing $\pm$ 1 standard error. Results from the pitch-angle–time analysis generally follow those from the energy–time analysis across events, despite the two methods relying on different assumptions: the energy–time method assumes instantaneous release of field-aligned electrons at all energies over a range of altitudes, while the pitch-angle method assumes an independent release at each energy, but with a broader pitch-angle distribution. When departures are visible (e.g. the 339 s event shown in Figure 4b), the differences in source altitude rarely surpass 1,000 km. This relatively good agreement between the two types of methods strengthens the confidence in the estimated source altitudes.

We observe variations in the range of source altitudes between events. For example, the event at 334 s (Figure 4c) is best represented with a quadratic fit very close to the linear fit, suggesting a narrow range of source altitudes (around 2,200 km) across all energies, consistent with results from the pitch-angle analysis. For this event, the quadratic fit is slightly concave, i.e.

https://doi.org/10.5194/egusphere-2026-2126
Preprint. Discussion started: 8 May 2026

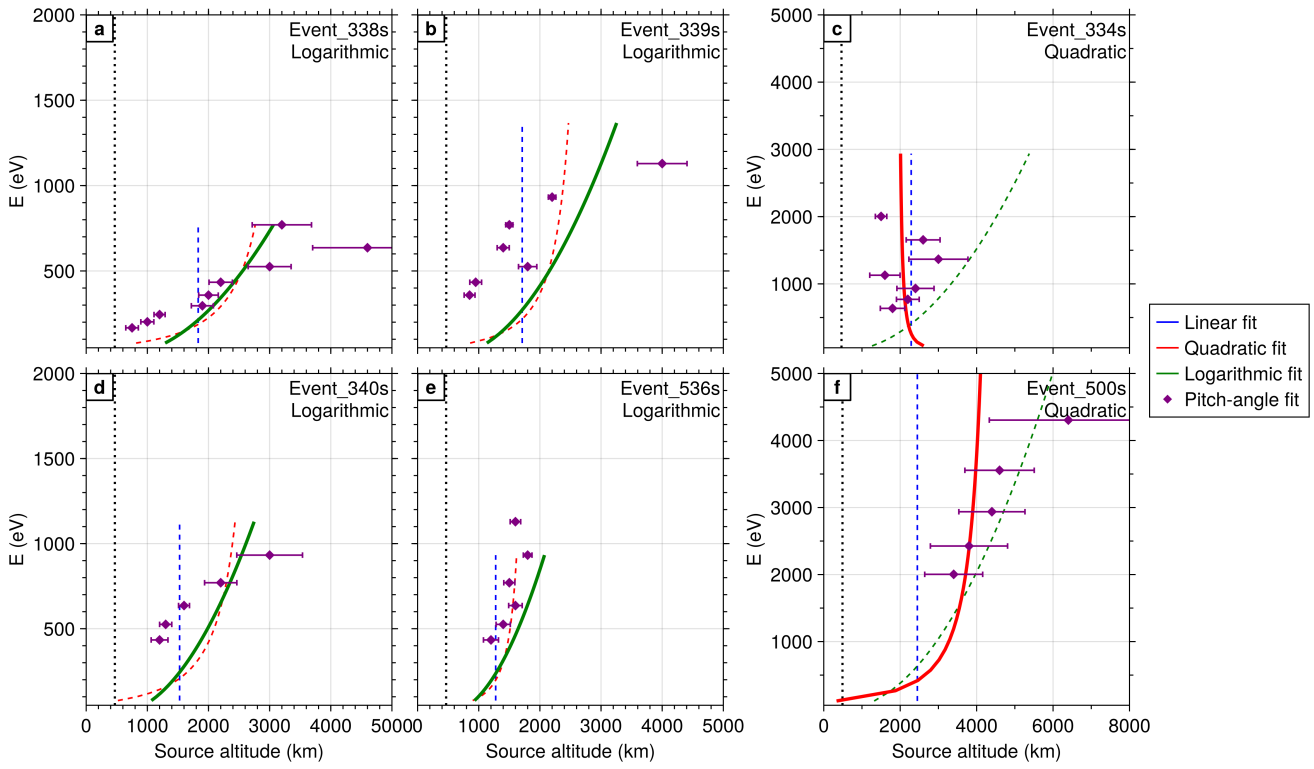

Figure 4. Results of the energy–time dispersion and pitch-angle–time dispersion analysis on a subset of events where both methods were applied. Each panel shows a different event whose time in the flight is indicated in the top-right corner. The blue, red and green curves indicate the source altitude as a function of energy for the linear, quadratic and logarithmic fits of the energy–time dispersions, respectively. The best model as found with the AICc is indicated in each panel with a solid line, while the two others are indicated by dashed lines. In addition, the name of the best model is also indicated in the top-right corner of each panel. Purple points indicate source altitude found with the pitch-angle–time dispersion modelling. Error bars indicate $\pm$ 1 standard error in the source altitude estimation. The rocket altitude is shown in each panel with a vertical dotted black line.

https://doi.org/10.5194/egusphere-2026-2126
Preprint. Discussion started: 8 May 2026

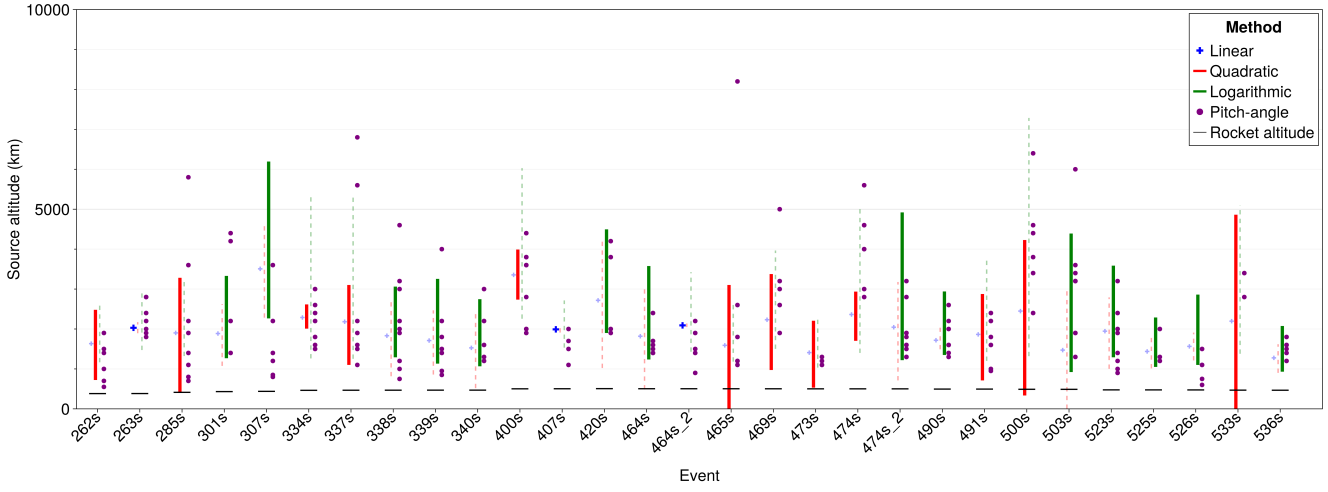

Figure 5. Summary of results of the energy–time dispersion and pitch-angle–time dispersion analysis applied to 29 events. The blue crosses indicate the source altitude from linear fit. The red and green lines indicate the range of source altitude found from the quadratic and logarithmic fits, respectively. The preferred model as found with the AICc is indicated with thicker lines and crosses. The purple dots indicate the source altitudes found with the pitch-angle method. The rocket altitude at the time of each measurement is indicated by a thin horizontal black line.

its coefficient b is positive and it bends in the other way than for the other events visible in Figure 4. This is consistent with the observations of Tanaka et al. (2005) finding the quadratic curves to be in general convex, but with a few events being concave close to linear. By contrast, the event at 338 s (Figure 4a) is best represented by a logarithmic fit, with source altitudes spanning a wider range (1,400 to 3,000 km), also supported by the pitch-angle analysis. The general trend is however that the source altitude increases with electron energy. For all events, the fitted t_{offset} parameter from the pitch-angle analysis tend to increase (not shown here) with the inverse of the electron energy, indicating a later time of release for the lower energy electrons. This is consistent with the source altitudes profiles shown in Figure 4 and the picture of a wave travelling down along the magnetic field line.

In Figure 5, we show a summary of the source altitude estimations across a large number of events for which energy–time and pitch-angle–time dispersions were easy to distinguish visually. Results from different energies are mixed, and the time of each event is indicated on the x-axis. Blue crosses show the source altitude from the linear TOF. Red and green lines indicate the range of source altitude from the quadratic and logarithmic fits, respectively. For each event, the preferred model according to the AICc is indicated with thicker lines and crosses. Purple dots show the source altitudes inferred from the pitch-angle forward model, and short horizontal bars indicate the rocket altitude at the time of the measurements.

With 12/29 events best fitted by a quadratic curve, 14/29 events best fitted by a logarithmic curve, and 3/29 events best fitted by a linear curve, we observe that the non-linear fits are generally preferred to the linear fit, consistent with the findings of Tanaka et al. (2005) and Feltman et al. (2025). Varying the lower energy cut-off described in Section 3.1 (set at 70 eV for the

https://doi.org/10.5194/egusphere-2026-2126
Preprint. Discussion started: 8 May 2026

results shown in Figure 5) with values from 50 eV to 100 eV makes the best fitting model for some event to switch from one curve to another. The general distribution of the favoured models and the range of source altitudes for each event is however generally unchanged.

It can be observed that for some events, the quadratic model infers source altitude for low-energy electrons below the rocket altitude, which is unphysical. This occurs because the local derivative of the quadratic $\Delta t(1/v)$ curve can become negative at low $1/v$ values, yielding negative source distances at the lowest energies.

As already noted with the few events presented in Figure 4, we also observe that the range of source altitudes found with the pitch-angle method generally agree with those from the energy TOF methods, though some outliers at lower and higher altitudes are visible. We also notice that the grand majority of source altitude found across event lays lower than 5,000 km, frequently between 1,000 and 3,000 km. We will discuss these findings in the light of other studies and theoretical expectations in the next section.

5 Discussion

5.1 Reliability of the source altitude estimations

To infer at which altitude the acceleration of the electrons took place, we have used two types of methods, one based on energy–time dispersions and one on pitch-angle–time dispersions. Both approaches are subject to uncertainties, which we discuss below.

The first source of uncertainty relates to the finite resolution of measurements. The energy–time dispersions methods rely on fitting the arrival times of electrons at different energies. However, as can be seen in Figure 2, the observed structures are often only a few pixels wide in time at each energy. Although we mitigate this by calculating a weighted mean, the limited time resolution still introduces uncertainty on the precise arrival time of each energy. We expect a higher temporal resolution to help constrain the dispersion fits and the inferred source altitudes. Similarly, the pitch-angle method is also affected by the measurement resolution. This is visible in Figure 4, where the uncertainties generally increase with source altitude (e.g. the large error bars in the 500 s event in Figure 4f). This increase reflects the reduced sensitivity of the pitch-angle–time dispersion shape to source altitude at large distances. Higher resolution measurements in time and/or pitch-angle would help better constrain the forward model and reduce these uncertainties.

A second source of uncertainty concerns the interpretation made of the dispersed structures themselves: do they reflect temporal variations in the precipitation, or spatial structures sampled by the moving spacecraft. This distinction is a long-standing question in in-situ observational studies of auroral precipitation (e.g. Tanaka et al., 2005; Wu et al., 2021). During the measurements, the rocket had a horizontal velocity of 1-2 km s^{-1}, implying that it covered spatial distances of roughly 0.5 to 1 km over the typical duration of these structures (< 0.5 s). Previous multi-point measurements studies have reported simultaneous measurement of similar precipitation signatures across payloads separated by $\sim$ 0.9-3 km (Arnoldy et al., 1999; Lynch et al., 1999, 2012), suggesting that these structures extend over larger spatial scale than the displacement of the rocket and therefore supporting a temporal interpretation. In addition, the coincident observation of dispersions in both energy and

https://doi.org/10.5194/egusphere-2026-2126
Preprint. Discussion started: 8 May 2026

pitch-angle (Figure 1) further strengthens a temporal origin (Arnoldy et al., 1999), as a purely spatial interpretation would imply simultaneous change across all pitch-angles.

A third source of uncertainty arise from the assumptions underlying each method. When deriving source altitudes from the energy–time dispersion fits, it is assumed that field-aligned electrons are released simultaneously over the whole source region, which is not fully consistent with the expected picture of a moving wave-particle interaction (Andersson et al., 2002). For the linear fit case, commonly used in the literature, this release is further assumed to occur from a single point. Similar to Tanaka et al. (2005) and Feltman et al. (2025), we find that the non-linear fits of the energy–time dispersions are generally preferred over the linear fits, supporting the case of a wider range of source altitude. Nevertheless, we also observe that the point source altitudes inferred from the linear fits typically fall near the middle of the altitude ranges derived from the non-linear fits (Figure 4, Figure 5). As such, it seems that the linear fit can provide a convenient first-order estimate, straightforward to compute, and that can be used for a quick comparisons across events and studies.

In order to relax the assumption of simultaneous release associated with the energy–time dispersions fits, we developed and applied a second method based on the pitch-angle–time dispersions. This approach allows the source altitude to be estimated independently for each electron energy, and instead assumes the instantaneous release of a broader pitch-angle distribution. We expect this assumption to be more accurate the higher the source altitudes. Indeed, at greater source distances, the injected electrons have a narrower pitch-angle distribution and are therefore more likely to originate from a similar altitude. For instance, the source altitude of the 4,300 eV electrons of the 500 s event (Figure 4f) is inferred to be around 6,400 km, with pitch-angles at the source ranging from 0° to 25°, meaning that all the electrons had a field-aligned velocity component between $\cos(25°) \approx 0.9$ and 1 of their total speed.

Despite the aforementioned uncertainties, we found both approaches, each with different underlying assumptions regarding electron injection, to yield comparable ranges of source altitudes across events (Figure 4 and Figure 5). This agreement between the two types of methods increases confidence in the inferred source altitudes.

5.2 Source altitudes in the context of previous studies

Having discussed the robustness and validity of the inferred source altitudes, we now examine how these results compare with previous observational studies and theoretical expectations.

The source altitudes inferred both from the energy–time and pitch-angle–time dispersions methods show some variability across events (Figure 4 and Figure 5), despite being observed during the same rocket flight. This suggests differences in the plasma conditions along nearby magnetic field lines. Whether these differences arise from local temporal variations or a larger spatial structuring of the acceleration region remains unclear due to space-time ambiguities than cannot be resolved with a single sounding rocket. It is expected that conditions along field lines can evolve following earlier auroral precipitation (Chaston et al., 2000, 2003b, 2006), but also that these regions can present strong spatial structuring, such as in the ionospheric Alfvén resonator (IAR) (Streltsov and Lotko, 2008).

Despite this variability, our observations generally indicate source altitudes of ∼1,000-3,000 km for electrons with energies of a few hundreds eV, and ∼2,000-5,000 km for electrons with energies of a few keV. The general trend is for high-energy

https://doi.org/10.5194/egusphere-2026-2126
Preprint. Discussion started: 8 May 2026

electrons to be released at higher altitudes than low-energy electrons, consistent with expected Alfvén velocity profiles along magnetic field lines (Chaston et al., 2002a). However, these values lie on the lower end of theoretical predictions (e.g. Kletzing and Hu, 2001; Chaston et al., 2003a), especially for the dayside (Chaston et al., 2003b).

For comparison, from their observations also made on the dayside at a similar MLT (around 13.3 MLT) with a sounding rocket, Tanaka et al. (2005) inferred source altitudes of ∼2,000-3,000 km for ∼30 eV electrons and ∼5,000-6,000 km for ∼200 eV electrons using a non-linear (quadratic) fit method. These values are more consistent with the theoretical estimations of Chaston et al. (2003b). However, the maximum electron energies in their dispersed structures were generally lower (a few hundreds eV) than in our observations (up to several keV), suggesting different conditions in the acceleration-region between our studies.

When compared with source altitudes reported in previous studies (Table 1) from linear fits of energy–time dispersions, our results also fall on the lower end of the observed range. Using the same linear fitting approach, our estimates typically lie between 1,000 and 3,000 km (blue crosses in Figure 5). However, similar source altitudes have been reported in Hirahara et al. (2024) as well as Mella et al. (2011) and Lynch et al. (2012) for events measured on the nightside and reaching several keV.

The results of Michell et al. (2025) were obtained using data from the Acute Precipitating Electron Spectrometer (APES) instrument (Michell et al., 2016) onboard the same rocket as in our study. By design, their instrument resolves primarily the highest energy part of the dispersions (Michell et al., 2025). The source altitudes of the 8 events they report range from approximately 1,700 km to 6,300 km, which is consistent with the higher-energy portion of the source altitudes we inferred from the non-linear energy fits and pitch-angle approaches presented here.

Overall, the wide range of source altitudes reported across studies (Table 1), from ∼500 m to several R_E, does not appear to clearly correlate with the spacecraft type (rocket vs satellite), the spacecraft altitude, or the magnetic local time (MLT) of observations. Similar to the event-to-event variations observed in our data, these differences suggest different plasma conditions along the magnetic field lines.

To further interpret our inferred source altitudes in terms of the plasma environment along the magnetic field lines, we compare our observations with theoretical expectations derived from different plasma density profiles in the acceleration region reported in the literature. Figure 6a shows the density profiles. All the profiles are based on the combination of an ionospheric exponential law for O^+ and a magnetospheric power-law component for H^+, with different parametrizations. The parametrizations of Kletzing et al. (1998), Chaston et al. (2002a) and Chaston et al. (2003a) result from statistical fits to spacecraft observations, whereas the parameters used by Thompson and Lysak (1996) and Lysak and Song (2008) were chosen to study specific plasma environments. In particular, the two profiles from Lysak and Song (2008) represent conditions inside and outside a density cavity. Figure 6b shows the magnetic field strength along the field line passing through the general rocket measurement region (taken at 76°N, 3°E and 100 km altitude), computed using the IGRF-14 model (International Association of Geomagnetism and Aeronomy, 2024). Figure 6c and Figure 6d show the corresponding electron skin-depth $\lambda_e = c/\omega_p$ and Alfvén velocity profiles (solid lines), together with inertial Alfvén wave velocity profiles (dashed lines). The inertial Alfvén velocities were computed assuming a perpendicular wavelength $\lambda_{\perp 0} = 5$ km at 200 km altitude (following Chaston et al., 2002a), scaled with $1/\sqrt{B}$ under the assumption of constant magnetic flux. This perpendicular scale should correspond to

https://doi.org/10.5194/egusphere-2026-2126
Preprint. Discussion started: 8 May 2026

Table 1. Comparison of source altitudes across studies found with the linear fit method of energy–time dispersions.

Study	Spacecraft	Altitude of s/c	Source altitude(s)	Conditions
McFadden et al. (1987)	BIDARCA (rockets)	310-565 km	4,000-8,000 km	Nightside (MLT 22)
Clemmons et al. (1994)	Freja (satellite)	1,750 km	2,600 km 6.7 R_E	Nightside (MLT 0345) Dusk (MLT 1714)
Arnoldy et al. (1999)	PHAZE-II (rocket)	950 km	3,500-5,300 km	Dusk (MLT 18.5)
Lynch et al. (1999)	AT2 (rocket)	545 km	10,000-20,000 km	Nightside (MLT 2100)
Andersson et al. (2002)	Freja (satellite)	1,700 km	0.7-1.4 R_E	Dayside (MLT 7.9-13.5)
Tanaka et al. (2005)	SS-520-2 (rocket)	550-1,100 km	2,000-6,000 km (avg. 3,773 km)	Dayside (MLT 13.3)
Mella et al. (2011) Lynch et al. (2012)	Cascades2 (rocket)	450-550 km	500-1,500 km	Nightside (MLT 2330)
Motoba and Hirahara (2016)	Reimei (satellite)	650 km	6,000 km	Nightside (MLT 00:20)
Hirahara et al. (2024)	Reimei (satellite)	675 km	1,700-2,700 km	Nightside (MLT 20.3)
Feltman et al. (2025)	ACES-II (rocket)	400 km	2,000-5,000 km	Dusk (MLT 19)
Michell et al. (2025)	VISIONS-2 (rocket)	550-600 km	1,700-6,300 km	Dayside (MLT 13.5)

auroral structures with optical widths of ∼1-2 km (Chaston et al., 2002a, 2003b). Figure 6e compares these theoretical profiles with the source altitudes inferred from our observations, with the inertial Alfvén wave velocities expressed as equivalent electron kinetic energies $E = \frac{1}{2} m_e v_{AI}^2$, which corresponds to the assumption that electrons are accelerated to approximately the local inertial Alfvén speed. These curves can as such be seen as lower bounds, as theoretical studies have shown that electrons accelerated through resonance interaction with IAW can reach energies greater than $1v_A$, up to $2v_A$ (e.g. Kletzing and Hu, 2001; Watt et al., 2005). The scatter points represent all source altitude estimates from Figure 5 as a function of electron energy, derived from the pitch-angle method (purple), the quadratic fit (red), and logarithmic fit (green).

https://doi.org/10.5194/egusphere-2026-2126
Preprint. Discussion started: 8 May 2026

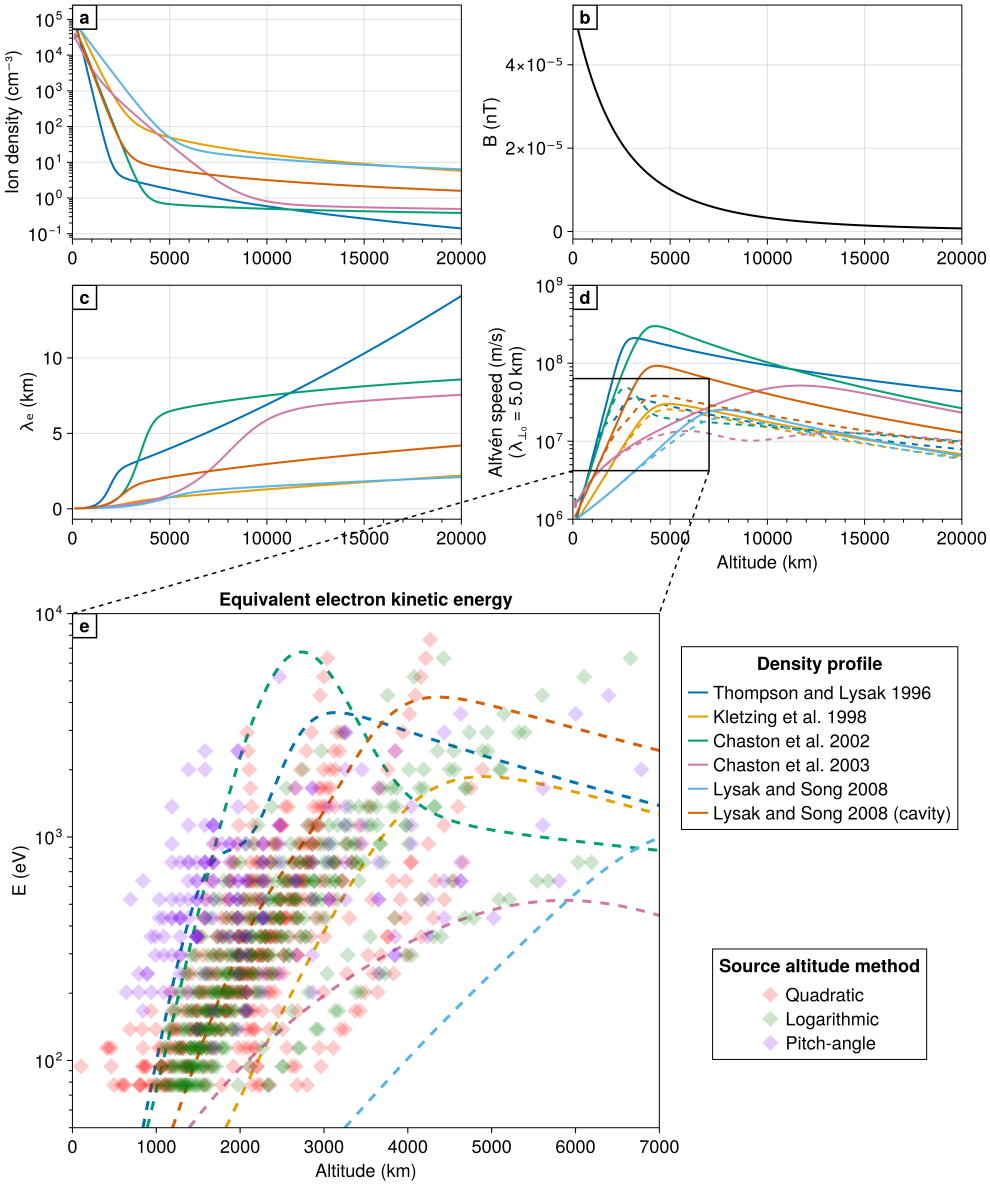

Figure 6. (a) Profiles of plasma density from the literature. (b) Profile of the magnetic field strength along the magnetic field line going through a point at 76° of latitude, 3° of longitude and 100 km of altitude, which corresponds to the region where the rocket is situated during the measurements. (c) Profiles of the electron skin-depth $\lambda_e = c/\omega_p$ obtained from the different density profiles. (d) Profiles of the corresponding Alfvén velocity (solid lines) and inertial Alfvén wave velocity (dashed lines). The inertial Alfvén wave velocities were calculated assuming a perpendicular wavelength of the wave $\lambda_{\perp 0}$ of 5 km (similar to Chaston et al. (2002a)) at 200 km of altitude, then scaled in altitude with $1/\sqrt{B}$ (constant magnetic flux assumption). (e) Zoom-in section of the velocity profiles from panel d. Only the inertial Alfvén waves profiles are shown. The y-axis values show what would be the equivalent kinetic electron energy calculated from $E = \frac{1}{2} m_e v_{AI}^2$. The scatter points show a compilation of all the source altitudes found as a function of energy for all the events shown in Figure 5 for the pitch-angle method (purple), quadratic fit (red) and logarithmic fit (green). All the results are mixed.

https://doi.org/10.5194/egusphere-2026-2126
Preprint. Discussion started: 8 May 2026

Using the parameters above-mentioned, the inferred source altitudes from our events are consistent with the IAW velocities predicted using the density profiles of Thompson and Lysak (1996) Kletzing et al. (1998), Chaston et al. (2002a), and the cavity profile of Lysak and Song (2008). A smaller number of events are also consistent with the profile of Chaston et al. (2003a), which is the results of a statistical fitting of dayside measurements. In contrast, almost none of our source altitudes follow the the outside-cavity conditions profile of Lysak and Song (2008). Taken together, the source altitudes inferred from our events are most consistent with profiles with the lowest plasma densities, which could correspond to auroral density cavity conditions. This picture is somewhat coherent with previous studies reporting observations from satellites between 1,000 and 4,000 km of altitude of Alfvén waves propagating inside density cavities and carrying intense parallel electric fields (Chaston et al., 1999, 2000, 2006, 2007b). A coupling between density cavities, Alfvén waves, and intense parallel electric fields that has been investigated and seemingly established in numerical studies (Génot et al., 2004; Lysak and Song, 2008; Mottez and Génot, 2011).

The comparison between inferred injection altitudes and the Alfvén-wave phase velocity profiles of Figure 6 suggests it is possible to fit the inferred energy, time, and height obtained from the pitch-angle dispersion fits described in Section 3.2 to the acceleration region parameters that influence the inertial Alfvén wave velocity: plasma density and perpendicular wavelength. We can build such a fit assuming a plasma density profile in the topside ionosphere of the following form (Lysak and Song, 2008)

$$n_{O^+} = n_0 e^{-z/H} \tag{2}$$

$$n_{H^+} = n_1 \left(\frac{z + R_E}{R_E} - 1 \right)^{-1} \tag{3}$$

$$n_e = n_{O^+} + n_{H^+} \tag{4}$$

with n_0 the O^+ density constant, n_1 the H^+ density constant, H the scale height of O^+, R_E the radius of the Earth, and z the geodetic height (vertical distance above ground). Quasi-neutrality is assumed, so that the electron density n_e is determined by the total ion density. The inertial Alfvén speed defined as

$$v_{AI} = \frac{v_A}{\sqrt{1 + k_\perp^2 \lambda_e^2}} \tag{5}$$

where $v_A = B/\sqrt{\mu_0 (n_{O^+} m_{O^+} + n_{H^+} m_{H^+})}$ is the pure MHD Alfvén velocity determined by O^+ and H^+ mass density and the IGRF magnetic field strength B, and $\lambda_e = c/\sqrt{n_e e^2 / m_e \epsilon_0}$ is the plasma skin-depth. The perpendicular wavenumber

$$k_\perp = \frac{2\pi}{\lambda_{\perp 0}} \sqrt{\frac{B}{B_0}} \tag{6}$$

is fixed by a perpendicular wavelength $\lambda_{\perp 0}$ and magnetic field strength B_0 defined at an altitude of 200 km and scaled by $1/\sqrt{B}$ assuming constant magnetic flux.

For each event, the pitch angle fit provides independent estimates of the source altitudes z_i for energy bins E_i. We assume that the release height of a discrete burst of Alfvénic precipitation with energy E is initiated at an altitude where the electron

https://doi.org/10.5194/egusphere-2026-2126
Preprint. Discussion started: 8 May 2026

energy is matched to the inertial Alfvén velocity, i.e., $Z(E, n_0, n_1, H, \lambda_{\perp 0}) = \arg\min_z |E - \frac{1}{2} m_e v_{AI}^2(z, n_0, n_1, H, \lambda_{\perp 0})|$. With this assumption it is now possible to search for plasma and wave parameters that best match the calculated source altitudes by minimizing the variance weighted sum of squares:

$$(\hat{n}_0, \hat{n}_1, \hat{H}, \hat{\lambda}_{\perp 0}) = \underset{n_0, n_1, H, \lambda_{\perp 0}}{\arg\min} \sum_i \sigma_i^{-2} \left| z_i - Z(E_i, n_0, n_1, H, \lambda_{\perp 0}) \right|^2 \tag{7}$$

where σ_i is the error standard deviation for the source height of energy bin i (error bars in Figure 4), and $(\hat{n}_0, \hat{n}_1, \hat{H}, \hat{\lambda}_{\perp 0})$ are the values of the best fit parameters.

Figure 7 shows this fitting technique applied to the pitch-angle estimated source altitudes of the 338 s event (same event as in Figures 2, 3, and 4a). Figure 7a shows the inferred source altitudes and their associated uncertainties (similar to Figure 4a). The black curve corresponds to the best fitting IAW speed curve to the points following equation 7. The values of the curve parameters are indicated in the top right corner of the panel, with their uncertainties computed with the same linearized uncertainty estimation technique as described in Section 3.2. The faint grey curves correspond to hundred IAW speed profiles computed by taking random samples around the best values of the four parameters $(n_0, n_1, H, \lambda_{\perp 0})$ using the linearized error covariance matrix of the estimated parameters. For this event, the fitted parameters are remarkably close to the values of the profiles from previous studies shown in Figure 6, as well as expected perpendicular IAW scales (Chaston et al., 2003b). Density profiles of O^+ and H^+ and $n_{tot} = n_{O^+} + n_{H+}$ along the field line can be reconstructed from the best fitting parameters following equations 2 and 3, as is shown in Figure 7b. The fitting technique was done on all the events shown in Figure 5, and approximately half of the cases were found to have fairly good, constrained fits as in Figure 7, while the others did not provide as clean fits.

The parameter estimation realized here is based on the simple assumption of electrons accelerated to $1 v_A$, as well as density profiles of the form of equations 2 and 3. It is a topic of future work to determine the most adequate assumptions and profile shapes, and if such fitting could be used reliably to infer topside plasma structuring.

https://doi.org/10.5194/egusphere-2026-2126
Preprint. Discussion started: 8 May 2026

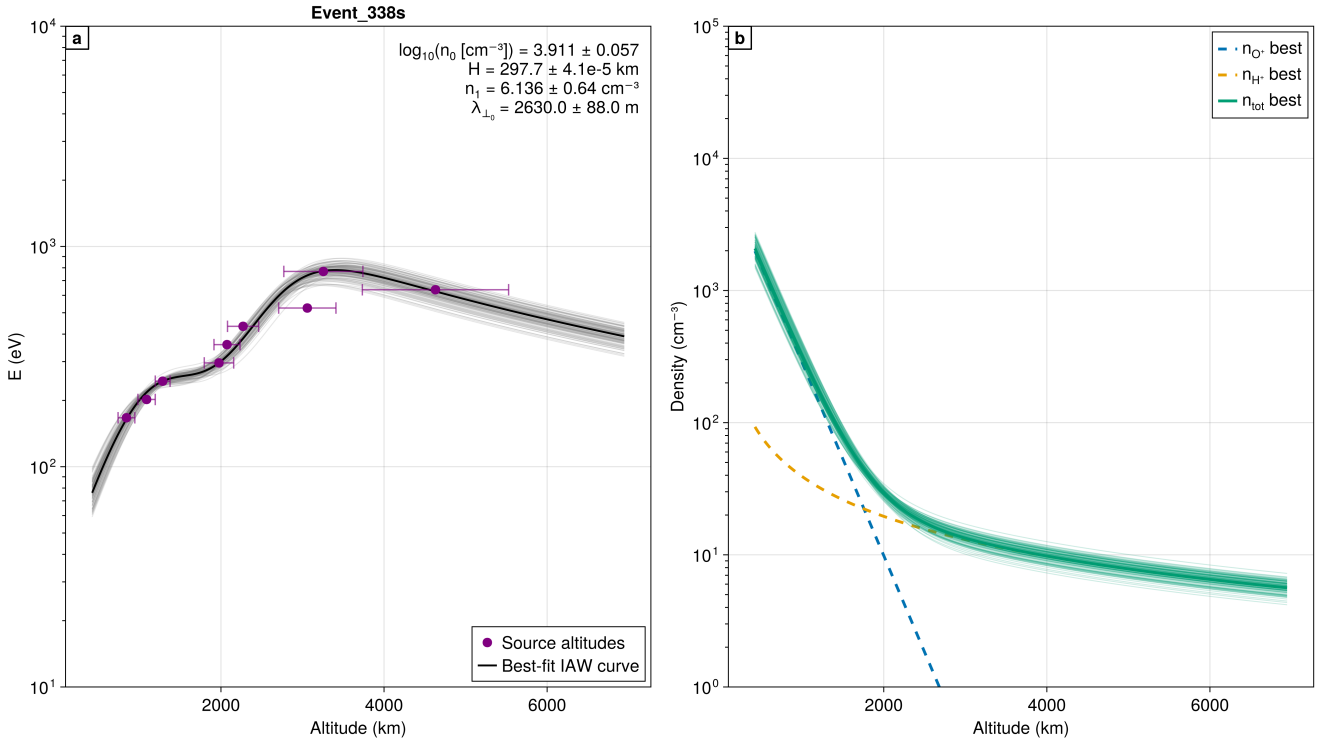

Figure 7. (a) Best-fit IAW speed profile (black curve) to the source altitudes estimated with the pitch-angle method applied to the event at 338 s. The values of the plasma and wave parameters and the associated uncertainties are indicated in the top-right corner. The faint grey curves correspond to IAW speed profiles computed by varying the parameters around their best value following the linearized error covariance matrix of the estimation. (b) Reconstructed density profiles corresponding to the IAW speed profiles of panel a.

6 Conclusions

In this study, we estimated the source altitude of auroral precipitation observed by the EESA top-hat instrument onboard the VISIONS-2 sounding rocket, launched on 7 December 2018 from Ny-Ålesund, Svalbard, into the active dayside auroral region (MLT ∼13.5 MLT). Numerous dispersed structures typical of auroral precipitation related to DAWs were observed. Their source altitude were inferred using the standard linear fit of energy–time dispersions which assumes a point release, but also using non-linear fits to obtain ranges of source altitude varying with energy. The non-linear curves were found to generally better fit the dispersions according to the AICc, similar to the findings of Tanaka et al. (2005), and supporting the hypothesis of an acceleration occurring across a range of altitudes.

In order to relax the assumption of simultaneous release of electrons from the whole range of source altitudes that is inherent to the energy–time dispersions fitting methods, we also developed a source altitude estimation method based on the forward modelling of pitch-angle–time dispersions. Using both complementary approaches, we obtained similar ranges of source alti-

https://doi.org/10.5194/egusphere-2026-2126
Preprint. Discussion started: 8 May 2026

tudes despite the different underlying assumptions. We observed the common trend across event of higher energies mapping to higher source altitudes. Despite some variation across events, we calculated around 70 % of the source altitudes of our observations inferred with the pitch-angle method to lie between 1,000 and 3,000 km (Figures 4 and 6e), for electrons with energies from hundreds of eV to a few keV. The variations in source altitudes observed across events suggest different conditions along the magnetic field lines where auroral acceleration takes place.

While on the lower range, the source altitudes we found generally agree with previous observations (Table 1) and theoretical profiles of the IAW velocity (Figure 6), especially those related to density cavities. The method discussed in Section 5.2. opens for the possibility to identify the best-fitting parameters for each event, and to extract the corresponding density profiles and perpendicular wave scale. This, combined with instrumental advancements offering higher-resolution measurements (e.g. Michell et al., 2016; Saito et al., 2017), could provide new clues about the plasma structures and processes occurring in the acceleration region.

Code and data availability. All data and scripts needed to reproduce the analysis and the figures are available at https://doi.org/10.5281/zenodo.19556096 (Gavazzi, 2026). Figures were made using *Makie.jl* (Danisch and Krumbiegel, 2021). The IGRF v14 model was computed using the Julia implementation of Chagas and Pantazides (2025).

Author contributions. EG, AS, BG and JV conceptualized the study and developed the methods. EG performed the analysis and made all the figures. DR is the PI of the rocket. JC and RP provided the electron flux data and the electric/magnetic field data, respectively. EG prepared the original draft. EG, AS, BG and JV reviewed and edited the final manuscript.

Competing interests. The authors declare that they have no conflict of interest.

Acknowledgements. Authors acknowledge the Norwegian contribution to the EISCAT project funded by the Research Council of Norway (RCN) through research infrastructure grant 350179. AS acknowledges funding from the RCN grant 326039 during part of the project. JC gratefully acknowledges support of the VISIONS-2 experiment by NASA through Grant NNX16AF02G. DR acknowledges support from the NASA ROSES Heliophysics Technology and Instrument Development for Science program and the NASA Sounding Rocket Program. RP and DR gratefully acknowledge support from NASA's Science Mission Directorate which enabled these experiments to be carried out.

https://doi.org/10.5194/egusphere-2026-2126
Preprint. Discussion started: 8 May 2026

References

Akaike, H.: A new look at the statistical model identification, IEEE Transactions on Automatic Control, 19, 716–723, https://doi.org/10.1109/TAC.1974.1100705, 1974.

Andersson, L., Ivchenko, N., Clemmons, J., Namgaladze, A. A., Gustavsson, B., Wahlund, J.-E., Eliasson, L., and Yurik, R. Y.: Electron signatures and Alfvén waves, Journal of Geophysical Research: Space Physics, 107, SMP 15–1–SMP 15–14, https://doi.org/10.1029/2001JA900096, _eprint: https://onlinelibrary.wiley.com/doi/pdf/10.1029/2001JA900096, 2002.

Arnoldy, R. L., Lynch, K. A., Austin, J. B., and Kintner, P. M.: Energy and pitch angle-dispersed auroral electrons suggesting a time-variable, inverted-V potential structure, Journal of Geophysical Research: Space Physics, 104, 22 613–22 621, https://doi.org/10.1029/1999JA900219, _eprint: https://agupubs.onlinelibrary.wiley.com/doi/pdf/10.1029/1999JA900219, 1999.

Aster, R. C., Borchers, B., and Thurber, C. H.: Parameter estimation and inverse problems, Elsevier, Amsterdam Oxford Cambridge, third edition edn., ISBN 978-0-12-804651-7, 2019.

Cameron, T. and Knudsen, D.: Inverse electron energy dispersion from moving auroral forms, Journal of Geophysical Research: Space Physics, 121, https://doi.org/10.1002/2016JA023045, 2016.

Carlson, C. W., Curtis, D. W., Paschmann, G., and Michel, W.: An instrument for rapidly measuring plasma distribution functions with high resolution, Advances in Space Research, 2, 67–70, https://doi.org/10.1016/0273-1177(82)90151-X, 1982.

Cavanaugh, J. E. and Neath, A. A.: The Akaike information criterion: Background, derivation, properties, application, interpretation, and refinements, WIREs Computational Statistics, 11, e1460, https://doi.org/10.1002/wics.1460, _eprint: https://wires.onlinelibrary.wiley.com/doi/pdf/10.1002/wics.1460, 2019.

Chagas, R. A. J. and Pantazides, A.: JuliaSpace/SatelliteToolboxGeomagneticField.jl: v1.2.0, https://doi.org/10.5281/zenodo.17273749, 2025.

Chaston, C. C., Carlson, C. W., Peria, W. J., Ergun, R. E., and McFadden, J. P.: FAST Observations of Inertial Alfven Waves in the Dayside Aurora, Geophysical Research Letters, 26, 647–650, https://doi.org/10.1029/1998GL900246, _eprint: https://agupubs.onlinelibrary.wiley.com/doi/pdf/10.1029/1998GL900246, 1999.

Chaston, C. C., Carlson, C. W., Ergun, R. E., and McFadden, J. P.: Alfvén Waves, Density Cavities and Electron Acceleration Observed from the FAST Spacecraft, Physica Scripta, 2000, 64, https://doi.org/10.1238/Physica.Topical.084a00064, 2000.

Chaston, C. C., Bonnell, J. W., Carlson, C. W., Berthomier, M., Peticolas, L. M., Roth, I., McFadden, J. P., Ergun, R. E., and Strangeway, R. J.: Electron acceleration in the ionospheric Alfven resonator, Journal of Geophysical Research: Space Physics, 107, SMP 41–1–SMP 41–16, https://doi.org/10.1029/2002JA009272, _eprint: https://onlinelibrary.wiley.com/doi/pdf/10.1029/2002JA009272, 2002a.

Chaston, C. C., Bonnell, J. W., Peticolas, L. M., Carlson, C. W., McFadden, J. P., and Ergun, R. E.: Driven Alfven waves and electron acceleration: A FAST case study, Geophysical Research Letters, 29, 30–1–30–4, https://doi.org/10.1029/2001GL013842, _eprint: https://agupubs.onlinelibrary.wiley.com/doi/pdf/10.1029/2001GL013842, 2002b.

Chaston, C. C., Bonnell, J. W., Carlson, C. W., McFadden, J. P., Ergun, R. E., and Strangeway, R. J.: Properties of small-scale Alfvén waves and accelerated electrons from FAST, Journal of Geophysical Research: Space Physics, 108, 2002JA009 420, https://doi.org/10.1029/2002JA009420, 2003a.

Chaston, C. C., Peticolas, L. M., Bonnell, J. W., Carlson, C. W., Ergun, R. E., McFadden, J. P., and Strangeway, R. J.: Width and brightness of auroral arcs driven by inertial Alfven waves, Journal of Geophysical Research: Space Physics, 108, 2001JA007 537, https://doi.org/10.1029/2001JA007537, 2003b.

https://doi.org/10.5194/egusphere-2026-2126
Preprint. Discussion started: 8 May 2026

Chaston, C. C., Genot, V., Bonnell, J. W., Carlson, C. W., McFadden, J. P., Ergun, R. E., Strangeway, R. J., Lund, E. J., and Hwang, K. J.: Ionospheric erosion by Alfvén waves, Journal of Geophysical Research: Space Physics, 111, https://doi.org/10.1029/2005JA011367, _eprint: https://onlinelibrary.wiley.com/doi/pdf/10.1029/2005JA011367, 2006.

Chaston, C. C., Carlson, C. W., McFadden, J. P., Ergun, R. E., and Strangeway, R. J.: How important are dispersive Alfvén waves for auroral particle acceleration?, Geophysical Research Letters, 34, L07 101, https://doi.org/10.1029/2006GL029144, 2007a.

Chaston, C. C., Hull, A. J., Bonnell, J. W., Carlson, C. W., Ergun, R. E., Strangeway, R. J., and McFadden, J. P.: Large parallel electric fields, currents, and density cavities in dispersive Alfvén waves above the aurora, Journal of Geophysical Research: Space Physics, 112, https://doi.org/10.1029/2006JA012007, _eprint: https://agupubs.onlinelibrary.wiley.com/doi/pdf/10.1029/2006JA012007, 2007b.

Chen, L.-J., Kletzing, C. A., Hu, S., and Bounds, S. R.: Auroral electron dispersion below inverted-V energies: Resonant deceleration and acceleration by Alfvén waves, Journal of Geophysical Research: Space Physics, 110, https://doi.org/10.1029/2005JA011168, _eprint: https://agupubs.onlinelibrary.wiley.com/doi/pdf/10.1029/2005JA011168, 2005.

Clemmons, J. H., Boehm, M. H., Paschmann, G. E., and Haerendel, G.: Signatures of energy-time dispersed electron fluxes measured by Freja, Geophysical Research Letters, 21, 1899–1902, https://doi.org/10.1029/94GL00885, _eprint: https://agupubs.onlinelibrary.wiley.com/doi/pdf/10.1029/94GL00885, 1994.

Danisch, S. and Krumbiegel, J.: Makie.jl: Flexible high-performance data visualization for Julia, Journal of Open Source Software, 6, 3349, https://doi.org/10.21105/joss.03349, 2021.

Feltman, C., Howes, G. G., Bounds, S. R., Miles, D. M., Kletzing, C. A., Greene, K., Broadfoot, R., Bonnell, J., and Roglans, R.: Inferential Evidence for Suprathermal Electron Burst Intensification Due To Inverted-V Precipitation via Inertial Alfvén Waves, Journal of Geophysical Research: Space Physics, 130, e2025JA033 869, https://doi.org/10.1029/2025JA033869, _eprint: https://agupubs.onlinelibrary.wiley.com/doi/pdf/10.1029/2025JA033869, 2025.

Gavazzi, E.: Replication material for "Estimating the source altitude of auroral precipitation from dispersed Alfvén waves in the dayside ionosphere", https://doi.org/10.5281/zenodo.19556096, 2026.

Gavazzi, E., Spicher, A., Gustavsson, B., Clemmons, J., Pfaff, R., and Rowland, D.: Time-dependent modeling of Alfvénic precipitation observed in the ionosphere, Annales Geophysicae, 44, 1–15, https://doi.org/10.5194/angeo-44-1-2026, 2026.

Goertz, C. K. and Boswell, R. W.: Magnetosphere-ionosphere coupling, Journal of Geophysical Research: Space Physics, 84, 7239–7246, https://doi.org/10.1029/JA084iA12p07239, _eprint: https://agupubs.onlinelibrary.wiley.com/doi/pdf/10.1029/JA084iA12p07239, 1979.

Génot, V., Louarn, P., and Mottez, F.: Alfvén wave interaction with inhomogeneous plasmas: acceleration and energy cascade towards small-scales, Annales Geophysicae, 22, 2081–2096, https://doi.org/10.5194/angeo-22-2081-2004, 2004.

Hasegawa, A.: Particle acceleration by MHD surface wave and formation of aurora, Journal of Geophysical Research (1896-1977), 81, 5083–5090, https://doi.org/10.1029/JA081i028p05083, _eprint: https://agupubs.onlinelibrary.wiley.com/doi/pdf/10.1029/JA081i028p05083, 1976.

Hirahara, M., Ebihara, Y., Kitamura, N., Sakanoi, T., Asamura, K., Takada, T., and Saito, H.: Reimei Satellite Observations of Alfvénic Interaction Modulating Inverted-V Electrons and Filamentary Auroral Forms at the Poleward Edge of a Discrete Arc, Journal of Geophysical Research: Space Physics, 129, e2024JA032 650, https://doi.org/10.1029/2024JA032650, _eprint: https://agupubs.onlinelibrary.wiley.com/doi/pdf/10.1029/2024JA032650, 2024.

Hui, C. H. and Seyler, C. E.: Electron acceleration by Alfvén waves in the magnetosphere, Journal of Geophysical Research: Space Physics, 97, 3953–3963, https://doi.org/10.1029/91JA03101, _eprint: https://agupubs.onlinelibrary.wiley.com/doi/pdf/10.1029/91JA03101, 1992.

International Association of Geomagnetism and Aeronomy: IGRF-14, https://doi.org/10.5281/zenodo.14218973, 2024.

https://doi.org/10.5194/egusphere-2026-2126
Preprint. Discussion started: 8 May 2026

Kataoka, R., Chaston, C. C., Knudsen, D., Lynch, K. A., Lysak, R. L., Song, Y., Rankin, R., Murase, K., Sakanoi, T., Semeter, J., Watanabe, T.-H., and Whiter, D.: Small-Scale Dynamic Aurora, Space Science Reviews, 217, 17, https://doi.org/10.1007/s11214-021-00796-w, 2021.

Kletzing, C. A.: Electron acceleration by kinetic Alfvén waves, Journal of Geophysical Research: Space Physics, 99, 11 095–11 103, https://doi.org/10.1029/94JA00345, _eprint: https://agupubs.onlinelibrary.wiley.com/doi/pdf/10.1029/94JA00345, 1994.

Kletzing, C. A. and Hu, S.: Alfvén wave generated electron time dispersion, Geophysical Research Letters, 28, 693–696, https://doi.org/10.1029/2000GL012179, _eprint: https://onlinelibrary.wiley.com/doi/pdf/10.1029/2000GL012179, 2001.

Kletzing, C. A. and Torbert, R. B.: Electron time dispersion, Journal of Geophysical Research: Space Physics, 99, 2159–2172, https://doi.org/10.1029/93JA01745, _eprint: https://agupubs.onlinelibrary.wiley.com/doi/pdf/10.1029/93JA01745, 1994.

Kletzing, C. A., Mozer, F. S., and Torbert, R. B.: Electron temperature and density at high latitude, Journal of Geophysical Research: Space Physics, 103, 14 837–14 845, https://doi.org/10.1029/98JA00962, _eprint: https://agupubs.onlinelibrary.wiley.com/doi/pdf/10.1029/98JA00962, 1998.

Lynch, K. A., Pietrowski, D., Torbert, R. B., Ivchenko, N., Marklund, G., and Primdahl, F.: Multiple-point electron measurements in a nightside auroral arc: Auroral turbulence II particle observations, Geophysical Research Letters, 26, 3361–3364, https://doi.org/10.1029/1999GL900599, _eprint: https://agupubs.onlinelibrary.wiley.com/doi/pdf/10.1029/1999GL900599, 1999.

Lynch, K. A., Hampton, D., Mella, M., Zhang, B., Dahlgren, H., Disbrow, M., Kintner, P. M., Lessard, M., Lundberg, E., and Stenbaek-Nielsen, H. C.: Structure and dynamics of the nightside poleward boundary: Sounding rocket and ground-based observations of auroral electron precipitation in a rayed curtain, Journal of Geophysical Research: Space Physics, 117, https://doi.org/10.1029/2012JA017691, _eprint: https://agupubs.onlinelibrary.wiley.com/doi/pdf/10.1029/2012JA017691, 2012.

Lysak, R. L.: Kinetic Alfvén waves and auroral particle acceleration: a review, Reviews of Modern Plasma Physics, 7, 6, https://doi.org/10.1007/s41614-022-00111-2, 2023.

Lysak, R. L. and Song, Y.: Propagation of kinetic Alfvén waves in the ionospheric Alfvén resonator in the presence of density cavities, Geophysical Research Letters, 35, https://doi.org/10.1029/2008GL035728, _eprint: https://agupubs.onlinelibrary.wiley.com/doi/pdf/10.1029/2008GL035728, 2008.

McFadden, J. P., Carlson, C. W., Boehm, M. H., and Hallinan, T. J.: Field-aligned electron flux oscillations that produce flickering aurora, Journal of Geophysical Research: Space Physics, 92, 11 133–11 148, https://doi.org/10.1029/JA092iA10p11133, _eprint: https://agupubs.onlinelibrary.wiley.com/doi/pdf/10.1029/JA092iA10p11133, 1987.

Mella, M. R., Lynch, K. A., Hampton, D. L., Dahlgren, H., Kintner, P. M., Lessard, M., Lummerzheim, D., Lundberg, E. T., Nicolls, M. J., and Stenbaek-Nielsen, H. C.: Sounding rocket study of two sequential auroral poleward boundary intensifications, Journal of Geophysical Research: Space Physics, 116, https://doi.org/10.1029/2011JA016428, _eprint: https://agupubs.onlinelibrary.wiley.com/doi/pdf/10.1029/2011JA016428, 2011.

Michell, R. G., Samara, M., Grubbs II, G., Ogasawara, K., Miller, G., Trevino, J. A., Webster, J., and Stange, J.: APES: Acute Precipitating Electron Spectrometer—A high time resolution monodirectional magnetic deflection electron spectrometer, Journal of Geophysical Research: Space Physics, 121, 5959–5965, https://doi.org/10.1002/2016JA022637, _eprint: https://agupubs.onlinelibrary.wiley.com/doi/pdf/10.1002/2016JA022637, 2016.

Michell, R. G., Samara, M., Grubbs, G., Rowland, D., Pfaff, R., and Clemmons, J. H.: Ultra-Fast Measurements of Precipitating Electrons in Earth's Cusp—A Source of Flickering Aurora Near 1 RE, Geophysical Research Letters, 52, e2025GL117 522, https://doi.org/10.1029/2025GL117522, _eprint: https://agupubs.onlinelibrary.wiley.com/doi/pdf/10.1029/2025GL117522, 2025.

https://doi.org/10.5194/egusphere-2026-2126
Preprint. Discussion started: 8 May 2026

Motoba, T. and Hirahara, M.: High-resolution auroral acceleration signatures within a highly dynamic onset arc, Geophysical Research Letters, 43, 1793–1801, https://doi.org/10.1002/2015GL067580, _eprint: https://agupubs.onlinelibrary.wiley.com/doi/pdf/10.1002/2015GL067580, 2016.

Mottez, F. and Génot, V.: Electron acceleration by an Alfvénic pulse propagating in an auroral plasma cavity: ALFVÉN PULSE IN CAVITY, Journal of Geophysical Research: Space Physics, 116, n/a–n/a, https://doi.org/10.1029/2010JA016367, 2011.

Saito, Y., Yokota, S., Asamura, K., and Krieger, A.: High-speed MCP anodes for high time resolution low-energy charged particle spectrometers, Journal of Geophysical Research: Space Physics, 122, 1816–1830, https://doi.org/10.1002/2016JA023157, _eprint: https://agupubs.onlinelibrary.wiley.com/doi/pdf/10.1002/2016JA023157, 2017.

Stasiewicz, K., Bellan, P., Chaston, C., Kletzing, C., Lysak, R., Maggs, J., Pokhotelov, O., Seyler, C., Shukla, P., Stenflo, L., Streltsov, A., and Wahlund, J.-E.: Small Scale Alfvénic Structure in the Aurora, Space Science Reviews, 92, 423–533, https://doi.org/10.1023/A:1005207202143, 2000.

Streltsov, A. V. and Lotko, W.: Coupling between density structures, electromagnetic waves and ionospheric feedback in the auroral zone, Journal of Geophysical Research: Space Physics, 113, https://doi.org/10.1029/2007JA012594, _eprint: https://agupubs.onlinelibrary.wiley.com/doi/pdf/10.1029/2007JA012594, 2008.

Sugiura, N.: Further analysis of the data by Akaike's information criterion and the finite corrections: Further analysis of the data by akaike' s, Communications in Statistics - Theory and Methods, 7, 13–26, https://doi.org/10.1080/03610927808827599, _eprint: https://doi.org/10.1080/03610927808827599, 1978.

Takahashi, T., Spicher, A., Di Mare, F., Rowland, D. E., Pfaff, R. F., Collier, M. R., Clausen, L. B. N., and Moen, J. I.: Suppression of Ionospheric Irregularity Due to Auroral Particle Impact, Journal of Geophysical Research: Space Physics, 127, e2020JA028 725, https://doi.org/10.1029/2020JA028725, 2022.

Tanaka, H., Saito, Y., Asamura, K., Ishii, S., and Mukai, T.: High time resolution measurement of multiple electron precipitations with energy-time dispersion in high-latitude part of the cusp region, Journal of Geophysical Research: Space Physics, 110, https://doi.org/10.1029/2004JA010664, _eprint: https://agupubs.onlinelibrary.wiley.com/doi/pdf/10.1029/2004JA010664, 2005.

Thompson, B. J. and Lysak, R. L.: Electron acceleration by inertial Alfvén waves, Journal of Geophysical Research: Space Physics, 101, 5359–5369, https://doi.org/10.1029/95JA03622, _eprint: https://agupubs.onlinelibrary.wiley.com/doi/pdf/10.1029/95JA03622, 1996.

Watt, C. E. J. and Rankin, R.: Electron acceleration due to inertial Alfvén waves in a non-Maxwellian plasma, Journal of Geophysical Research: Space Physics, 112, https://doi.org/10.1029/2006JA011907, _eprint: https://agupubs.onlinelibrary.wiley.com/doi/pdf/10.1029/2006JA011907, 2007.

Watt, C. E. J. and Rankin, R.: Do magnetospheric shear Alfvén waves generate sufficient electron energy flux to power the aurora?, Journal of Geophysical Research: Space Physics, 115, https://doi.org/10.1029/2009JA015185, _eprint: https://agupubs.onlinelibrary.wiley.com/doi/pdf/10.1029/2009JA015185, 2010.

Watt, C. E. J., Rankin, R., Rae, I. J., and Wright, D. M.: Self-consistent electron acceleration due to inertial Alfvén wave pulses, Journal of Geophysical Research: Space Physics, 110, https://doi.org/10.1029/2004JA010877, _eprint: https://agupubs.onlinelibrary.wiley.com/doi/pdf/10.1029/2004JA010877, 2005.

Watt, C. E. J., Rankin, R., Rae, I. J., and Wright, D. M.: Inertial Alfvén waves and acceleration of electrons in nonuniform magnetic fields, Geophysical Research Letters, 33, https://doi.org/10.1029/2005GL024779, _eprint: https://agupubs.onlinelibrary.wiley.com/doi/pdf/10.1029/2005GL024779, 2006.

https://doi.org/10.5194/egusphere-2026-2126
Preprint. Discussion started: 8 May 2026

Wu, J., Knudsen, D. J., Shen, Y., and Gillies, D. M.: e-POP Observations of Suprathermal Electron Bursts in the Ionospheric Alfvén Resonator, Journal of Geophysical Research: Space Physics, 126, e2020JA028 005, https://doi.org/10.1029/2020JA028005, _eprint: https://agupubs.onlinelibrary.wiley.com/doi/pdf/10.1029/2020JA028005, 2021.

Wygant, J. R., Keiling, A., Cattell, C. A., Johnson, M., Lysak, R. L., Temerin, M., Mozer, F. S., Kletzing, C. A., Scudder, J. D., Peterson, W., Russell, C. T., Parks, G., Brittnacher, M., Germany, G., and Spann, J.: Polar spacecraft based comparisons of intense electric fields and Poynting flux near and within the plasma sheet-tail lobe boundary to UVI images: An energy source for the aurora, Journal of Geophysical Research: Space Physics, 105, 18 675–18 692, https://doi.org/10.1029/1999JA900500, 2000.